

New evidence for the saturation of the Froissart bound

M. M. Block

Department of Physics and Astronomy,
Northwestern University, Evanston, IL 60208

F. Halzen

Department of Physics,
University of Wisconsin, Madison, WI 53706

Abstract

Fits to high energy data alone cannot cleanly discriminate between asymptotic $\ln s$ and $\ln^2 s$ behavior of total hadronic cross sections. We demonstrate that this is no longer true when we require that these amplitudes also describe, on average, low energy data dominated by resonances. We simultaneously fit real analytic amplitudes to high energy measurements of: 1) the π^+p and π^-p total cross sections and ρ -values (ratio of the real to the imaginary portion of the forward scattering amplitude), for $\sqrt{s} \leq 6$ GeV, while requiring that the asymptotic fits smoothly join the π^+p and π^-p total cross sections at $\sqrt{s} = 2.6$ GeV both in magnitude and slope, and 2) separately simultaneously fit the pp and $\bar{p}p$ total cross sections and ρ -values for $\sqrt{s} \leq 6$ GeV, while requiring that their asymptotic fits smoothly join the pp and $\bar{p}p$ total cross sections at $\sqrt{s} = 4.0$ GeV again both in magnitude and slope. In both cases, we have used all of the extensive data of the PDG group [10]. However, we then subject these data to a screening process, the "Sieve" algorithm [1], in order to eliminate "outliers" that can skew a χ^2 fit. With the "Sieve" algorithm, a robust fit using a Lorentzian distribution is first made to all of the data to sieve out abnormally high χ^2_i , the individual i^{th} point's contribution to the total χ^2 . The χ^2 fits are then made to the sieved data. Both the p and nucleon-nucleon systems strongly favor a high energy $\ln^2 s$ fit of the form: $\sigma = c_0 + c_1 \ln \frac{\sqrt{s}}{m} + c_2 \ln^2 \frac{\sqrt{s}}{m} + \frac{p^0}{m} \frac{1}{m} \frac{1}{m}$, basically excluding a $\ln s$ fit of the form: $\sigma = c_0 + c_1 \ln \frac{\sqrt{s}}{m} + \frac{p^0}{m} \frac{1}{m} \frac{1}{m}$. The upper sign is for π^+p (pp) and the lower sign is for π^-p ($\bar{p}p$) scattering, where \sqrt{s} is the laboratory pion (proton) energy, and m is the pion (proton) mass.

High energy cross sections for the scattering of hadrons should be bounded by $\ln^2 s$, where s is the square of the cm s energy. This fundamental result is derived from unitarity and analyticity by Froissart [2], who states: "At forward or backward angles, the modulus of the amplitude behaves at most like $s \ln^2 s$, as s goes to infinity. We can use the optical theorem to derive that the total cross sections behave at most like $\ln^2 s$, as s goes to infinity". In this context, saturating the Froissart bound refers to an energy dependence of the total cross section rising no more rapidly than $\ln^2 s$.

The question as to whether any of the present day high energy data for pp, pp and $\bar{p}p$ cross sections saturate the Froissart bound has not been settled; one can not unambiguously discriminate between asymptotic fits of $\ln s$ and $\ln^2 s$ using high energy data only [3, 4]. We here point out that this ambiguity is resolved by requiring that the fits to the high energy data smoothly join the cross section and energy dependence obtained by averaging the resonances at low energy. Imposing this duality [5] condition, we show that only fits to the high energy data behaving as $\ln^2 s$ that smoothly join (in both magnitude and first derivative) to the low energy data at the "transition energy" (defined as the energy region just after the resonance regions end) can adequately describe the highest energy points. This technique has recently been successfully used by Block and Halzen [6] to show that the Froissart bound is saturated for the $\bar{p}p$ system.

We will use real analytic amplitudes to describe the data. Following Block and Cahn [7], we write the crossing-even real analytic amplitude for high energy scattering as [6], [8]

$$f_+ = i \frac{1}{4} A + [\ln(s=s_0) - i=2]^2 + c s^{-1} e^{i(\pi - \pi/2)} i \frac{1}{4} f_+(0) ; \quad (1)$$

and the crossing-odd amplitude as

$$f_- = D s^{-1} e^{i(\pi - \pi/2)} ; \quad (2)$$

where A, c, s_0 and D are real constants. The variable s is the square of the center of mass system (cm s) energy and π is the laboratory momentum. The additional real constant $f_+(0)$ is the subtraction constant at $\pi = 0$ needed to be introduced in a singly-subtracted dispersion relation [7], [9]. Using the optical theorem, we obtain the total cross section

$$\sigma_{\text{tot}} = A + \ln^2 s = s_0 + \frac{2}{4} + c \sin(\pi - \pi/2) s^{-1} D \cos(\pi - \pi/2) s^{-1} \quad (3)$$

with ρ , the ratio of the real to the imaginary part of the forward scattering amplitude, given by

$$\rho = \frac{1}{\sigma_{\text{tot}}} \ln s = s_0 + c \cos(\pi - \pi/2) s^{-1} + \frac{4}{4} f_+(0) D \sin(\pi - \pi/2) s^{-1} ; \quad (4)$$

where the upper sign is for $\bar{p}p$ (pp) and the lower sign is for $p\bar{p}$ (pp) scattering, and the even amplitude applies to the spin-averaged $\bar{p}p$ scattering [5].

We now introduce the definitions $A = c_0 + \frac{2}{4} c_2 \frac{c_1^2}{4c_2}, s_0 = 2m^2 e^{-c_1/(2c_2)}, \pi = c_2, c = \frac{(2m^2)^{1/2}}{\sin(\pi/2)} p^0$ and $D = \frac{(2m^2)^{1/2}}{\cos(\pi/2)}$. In the high energy limit, where $s \gg 2m^2$, Eq. (3) and Eq. (4), along with their cross section derivatives $\frac{d}{d(\pi - \pi/2)}$, can be written as

$$\sigma_{\text{tot}} = c_0 + c_1 \ln \frac{s}{m^2} + c_2 \ln^2 \frac{s}{m^2} + p^0 \frac{1}{m^2} \frac{1}{m^2} ; \quad (5)$$

$$\rho = \frac{1}{2} \frac{c_1 + c_2 \ln \frac{s}{m^2}}{p^0 \cot(\frac{\pi}{2}) \frac{1}{m^2}} + \frac{4}{4} f_+(0) \tan(\frac{\pi}{2}) \frac{1}{m^2} ; \quad (6)$$

$$\frac{d}{d(\pi - \pi/2)} = c_1 \frac{1}{(\pi - \pi/2)} + c_2 \frac{2 \ln(\pi - \pi/2)}{(\pi - \pi/2)} + p^0 (1)(\pi - \pi/2)^2 \quad (7)$$

$$(\pi - \pi/2)(\pi - \pi/2)^2 ; \quad (8)$$

where the upper sign is for $\bar{p}p$ (pp) and the lower sign is for $p\bar{p}$ (pp) scattering. The exponents π and $\pi/2$ are real. This transformation linearizes Eq. (5) in the real coefficients c_0, c_1, c_2, p^0 and π , convenient for a χ^2 fit to the experimental total cross sections and ρ -values. Throughout we will use units of GeV and cross section in mb, where m is the projectile mass.

Let σ^+ be the total cross section for π^+p (pp) scattering and σ^- the total cross section for π^-p (pp) scattering. It is convenient to define, at the transition energy E_0 ,

$$\begin{aligned} \sigma_{av} &= \frac{\sigma^+(E_0) + \sigma^-(E_0)}{2} \\ &= c_0 + c_1 \ln(E_0) + c_2 \ln^2(E_0) + \sigma^0(E_0)^{-1}; \end{aligned} \quad (9)$$

$$\begin{aligned} &= \frac{\sigma^+(E_0) - \sigma^-(E_0)}{2} \\ &= (E_0)^{-1}; \end{aligned} \quad (10)$$

$$\begin{aligned} m_{av} &= \frac{1}{2} \left(\frac{d\sigma^+}{d(E_0)} + \frac{d\sigma^-}{d(E_0)} \right)_{E_0} \\ &= c_1 \frac{1}{(E_0)} + c_2 \frac{2 \ln(E_0)}{(E_0)} + \sigma^0(E_0)^{-2}; \end{aligned} \quad (11)$$

$$\begin{aligned} m &= \frac{1}{2} \left(\frac{d\sigma^+}{d(E_0)} - \frac{d\sigma^-}{d(E_0)} \right)_{E_0} \\ &= (E_0)^{-2}; \end{aligned} \quad (12)$$

Using the definitions of σ_{av} , σ^- , m_{av} and m , we now write the four constraint equations

$$\sigma^0 = \frac{(E_0)^2}{1} m_{av} - c_1 \frac{1}{(E_0)} - c_2 \frac{2 \ln(E_0)}{(E_0)}; \quad (13)$$

$$c_0 = \sigma_{av} - c_1 \ln(E_0) - c_2 \ln^2(E_0) - \sigma^0(E_0)^{-1}; \quad (14)$$

$$= 1 + \frac{m}{(E_0)}; \quad (15)$$

$$= (E_0)^{-1}; \quad (16)$$

that utilize the two slopes and the two intercepts at the transition energy E_0 , where we join on to the asymptotic fit. We pick E_0 as the (very low) energy just after which resonance behavior finishes. We use $E_0 = 0.5$ throughout, which is appropriate for a Regge-descending trajectory. In the above, $m = m_p$ is the proton mass for the pp and πp systems, while $m = m_\pi$ is the pion mass for the πp and π^+p systems.

Our strategy is to use the rich amount of low energy data to constrain our high energy fit. At the transition energy E_0 , the cross sections $\sigma^+(E_0)$ and $\sigma^-(E_0)$, along with the slopes $\frac{d\sigma^+}{d(E_0)}_{E_0}$ and

$\frac{d\sigma^-}{d(E_0)}_{E_0}$, are used to constrain the asymptotic high energy fit so that it matches the low energy data at the transition energy E_0 . We pick E_0 much below the energy at which we start our high energy fit, but at an energy safely above the resonance regions. Very local fits are made to the region about the energy E_0 in order to evaluate the two cross sections and their two derivatives at E_0 that are needed in the above constraint equations. We next impose the 4 constraint equations, Equations (13), (14), (15) and (16), which we use in our χ^2 fit to Equations 5 and 6. For safety, we start the data fitting at an energy E_{min} appreciably higher than the transition energy. The transition energies, with appropriate cross sections and slopes, are summarized in Table 1, along with the minimum energies used in the asymptotic fits.

We stress that the odd amplitude parameters c_1 and c_2 and hence the odd amplitude itself is completely determined by the experimental values m and σ^- at the transition energy E_0 . Thus, at all energies, the differences of the cross sections $\sigma^+ - \sigma^-$ (from the optical theorem, the differences in the imaginary portion of the scattering amplitude) and the differences of the real portion of the scattering amplitude are completely fixed before we make our fit. Further, for a $\ln^2 s$ ($\ln s$) fit, the even amplitude parameters c_0 and σ^0 are determined by c_1 and c_2 (c_1 only) along with the experimental values of σ_{av} and m_{av} at the transition energy E_0 . In particular, for a $\ln^2 s$ ($\ln s$) fit, we only fit the 3 (2) parameters c_1 , c_2 , and $f_+(0)$ (c_1 and $f_+(0)$). Since the subtraction constant $f_+(0)$ only enters into the χ^2 -value determinations, only the 2 parameters c_1 and c_2 of the original 7 are required for a $\ln^2 s$ fit to the cross sections, which gives us exceedingly little freedom in this fit—it is indeed very tightly constrained, with not much latitude for adjustment. The cross sections for the $\ln s$ fit are even more tightly constrained, with only one adjustable parameter, c_1 .

We now outline the adaptive Sieve algorithm [1] that minimizes the effect that "outliers" | points with abnormally high contributions to χ^2 | have on a fit when they contaminate a data sample that is otherwise Gaussianly distributed. Our fitting procedure consists of several steps:

1. Make a robust fit of all of the data (presumed outliers and all) by minimizing χ^2_0 , the Lorentzian squared with respect to β , where

$$\chi^2_0(\beta; x) = \sum_{i=1}^N \ln [1 + 0.179 \frac{\chi^2_i(x_i; \beta)}{\beta}] ; \quad (17)$$

with $\beta = \beta_1; \dots; \beta_M$ being the M -dimensional parameter space of the fit. $x = x_1; \dots; x_N$ represents the abscissa of the N experimental measurements $y = y_1; \dots; y_N$ that are being fit and

$\chi^2_i(x_i; \beta) = \frac{y_i - y(x_i; \beta)}{\sigma_i}^2$ is the individual χ^2 contribution of the i^{th} point, where $y(x_i; \beta)$ is the theoretical value at x_i and σ_i is the experimental error. It is shown in ref. [1] that for Gaussianly distributed data, minimizing χ^2_0 gives, on average, the same total $\chi^2_{\text{min}} = \sum_{i=1}^N \chi^2_i(x_i; \beta)$ from Eq. (17) as that found in a conventional χ^2 fit, as well as the same widths (errors) for the parameters that are almost the same as those found in a χ^2 fit.

A quantitative measure of whether point i is an outlier, i.e., whether it is "far away" from the true signal, is the magnitude of its $\chi^2_i(x_i; \beta) = \frac{y_i - y(x_i; \beta)}{\sigma_i}^2$. The reason for minimizing the Lorentzian squared is that this procedure gives the outliers much less weight w in the fit ($w \propto 1/\chi^2_i(x_i; \beta)$), for large $\chi^2_i(x_i; \beta)$ than does a χ^2 fit ($w \propto 1/\chi^2_i(x_i; \beta)$), thus making the fitted parameters insensitive to outliers and hence robust. For details, see ref. [1].

If χ^2_{min} is satisfactory, make a conventional χ^2 fit to get the errors and you are finished. If χ^2_{min} is not satisfactory, proceed to step 2.

2. Using the above robust χ^2_0 fit as the initial estimator for the theoretical curve, evaluate $\chi^2_i(x_i; \beta)$, for each of the N experimental points.
3. A largest cut, $\chi^2_i(x_i; \beta)_{\text{max}}$, must now be selected. We start the process with $\chi^2_i(x_i; \beta)_{\text{max}} = 9$. If any of the points have $\chi^2_i(x_i; \beta) > \chi^2_i(x_i; \beta)_{\text{max}}$, reject them | they fell through the "Sieve". The choice of $\chi^2_i(x_i; \beta)_{\text{max}}$ is an attempt to pick the largest "Sieve" size (largest $\chi^2_i(x_i; \beta)_{\text{max}}$) that rejects all of the outliers, while minimizing the number of signal points rejected.
4. Next, make a conventional χ^2 fit to the sifted set | these data points are the ones that have been retained in the "Sieve". This fit is used to estimate χ^2_{min} . Since the data set has been truncated by eliminating the points with $\chi^2_i(x_i; \beta) > \chi^2_i(x_i; \beta)_{\text{max}}$, we must slightly renormalize the χ^2_{min} found to take this into account, by the factor R . For $\chi^2_{\text{max}} = 9; 6$; and 4 , the factor R is given by 1.027 , 1.140 and 1.291 , whereas the fraction of the points that should survive this χ^2 cut | for a Gaussian distribution | is 0.9973 , 0.9857 and 0.9545 , respectively. A plot of R^{-1} as a function of χ^2_{max} is given in Figure 1, which is taken from ref. [1].

If the renormalized χ^2_{min} , i.e., $R \chi^2_{\text{min}}$ is acceptable | in the conventional sense, using the ordinary χ^2 distribution probability function | we consider the fit of the data to the model to be satisfactory and proceed to the next step. If the renormalized χ^2_{min} is not acceptable and $\chi^2_i(x_i; \beta)_{\text{max}}$ is not too small, we pick a smaller $\chi^2_i(x_i; \beta)_{\text{max}}$ and go back to step 3. The smallest value of $\chi^2_i(x_i; \beta)_{\text{max}}$ that we used is $\chi^2_i(x_i; \beta)_{\text{max}} = 4$.

5. From the χ^2 fit that was made to the "sifted" data in the preceding step, evaluate the parameters. Next, evaluate the $M \times M$ covariance (squared error) matrix of the parameter space which was found in the χ^2 fit. We find the new squared error matrix for the χ^2 fit by multiplying the covariance matrix by the square of the factor r_2 . From Figure 1, we find that $r_2 = 1.02; 1.05$ and 1.11 for $\chi^2_i(x_i; \beta)_{\text{max}} = 9, 6$ and 4 , respectively. The values of $r_2 > 1$ reflect the fact that a χ^2 fit to the truncated Gaussian distribution that we obtain | after first making a robust fit | has a rms (root mean square) width which is somewhat greater than the rms width of the χ^2 fit to the same untruncated distribution [1].

The application of a χ^2 test to the sifted set gives stable estimates of the model parameters, as well as a goodness-of-fit of the data to the model when χ^2_{min} is renormalized for the effect of truncation due to the cut $\chi^2_{i, max}$. One can now use conventional probabilities for χ^2 tests, i.e., the probability that χ^2 is greater than $R \chi^2_{min}$, for the number of degrees of freedom ν . Model parameter errors are found by multiplying the covariance (squared error) matrix of the conventional χ^2 test by the appropriate factor $(R)^2$ for the cut $\chi^2_{i, max}$.

Table 2 summarizes the results of our simultaneous fits to all of the available data from the Particle Data Group [10] for $p\bar{p}$, $p\bar{p}$, $p\bar{p}$ and $p\bar{p}$, using the 4 constraint equations with a transition energy $\sqrt{s} = 2.6$ GeV and a minimum fitting energy of 6 GeV, after applying the "Sieve" algorithm [1]. Three $\chi^2_{i, max}$ cuts, 4, 6 and 9, were made for $\ln^2(\chi^2)$ tests. There was considerable improvement in the renormalized $\chi^2/d.f.$ going from $\chi^2_{i, max} = 9$ to $\chi^2_{i, max} = 6$. However, there was no improvement of the renormalized $\chi^2/d.f.$ going from $\chi^2_{i, max} = 6$ to $\chi^2_{i, max} = 4$; indeed, it increased from 1.294 to 1.364. Since the errors also become substantially larger for the $\chi^2_{i, max} = 4$ cut, we chose to use the values of the $\ln^2(\chi^2)$ test with a $\chi^2_{i, max} = 6$ cut. This cut was therefore also used for the $\ln(\chi^2)$ test. The probability of the fit for the data set using the $\chi^2_{i, max} = 6$ cut was 0.02, a somewhat low probability, albeit one that is often deemed acceptable in a fit with this many degrees of freedom ($d.f. = 127$). In contrast, the probability of the $\ln(\chi^2)$ test using the $\chi^2_{i, max} = 6$ data set is $< 10^{-16}$ and is clearly ruled out, as is graphically demonstrated in Fig. 2.

It should be noted that when using a $\ln^2(\chi^2)$ test before imposing the "Sieve" algorithm, a value of $\chi^2/d.f. = 3.472$ for 152 degrees of freedom was found, compared to $\chi^2/d.f. = 1.294$ for 127 degrees of freedom when using the $\chi^2_{i, max} = 6$ cut. In essence, the "Sieve" algorithm eliminated 25 points with energies $\sqrt{s} = 6$ GeV ($2 p\bar{p}$, $19 p\bar{p}$, $4 p\bar{p}$), while changing the total renormalized χ^2 from 527.8 to 164.3. These 25 points that were screened out had a χ^2 contribution of 363.5, an average value of 14.5. If the distribution had been Gaussian with no outliers, one would have expected about 2 points having $\chi^2_i > 6$, giving a total χ^2 contribution slightly larger than 12, compared to the observed value of 363.5. Thus, we see the effect of the "Sieve" algorithm in cleaning up the data sample by eliminating the outliers.

Next, we analyze the pp and $p\bar{p}$ systems. Table 3 summarizes the results of our simultaneous fits to the available accelerator data from the Particle Data Group [10] for pp , $p\bar{p}$, $p\bar{p}$ and $p\bar{p}$, using the 4 constraint equations with a transition energy $\sqrt{s} = 4$ GeV and a minimum fitting energy of 6 GeV, again using the "Sieve" algorithm. Two $\chi^2_{i, max}$ cuts, 6 and 9, were made for $\ln^2(\chi^2)$ tests. The probability of the fit for the cut $\chi^2_{i, max} = 6$ was 0.2, a very satisfactory probability for this many degrees of freedom, and we chose this data set rather than the data set corresponding to the $\chi^2_{i, max} = 9$ cut. As seen in Table 3, the fitted parameters are very insensitive to this choice. The same data set ($\chi^2_{i, max} = 6$ cut) was also used for the $\ln(\chi^2)$ test. The probability of the $\ln(\chi^2)$ test is $< 10^{-16}$ and is clearly ruled out. This is illustrated graphically in Fig. 6 and Fig. 7.

We note that when using a $\ln^2(\chi^2)$ test before imposing the "Sieve" algorithm, a value of $\chi^2/d.f. = 5.657$ for 209 degrees of freedom was found, compared to $\chi^2/d.f. = 1.095$ for 184 degrees of freedom when using the $\chi^2_{i, max} = 6$ cut. The "Sieve" algorithm eliminated 25 points with energies $\sqrt{s} = 6$ GeV ($5 pp$, $5 p\bar{p}$, $15 p\bar{p}$), while changing the total renormalized χ^2 from 1182.3 to 201.4. These 25 points that were screened out had a χ^2 contribution of 980.9, an average value of 39.2. For a Gaussian distribution, about 3 points with $\chi^2_i > 6$ are expected, with a total χ^2 contribution of slightly more than 18 and not 980.9. A gain, we see the effect of the "Sieve" algorithm in ridding the data sample of outliers.

Fig. 2 shows the individual fitted cross sections (in mb) for $p\bar{p}$ and $p\bar{p}$ for $\ln^2(\chi^2)$ and $\ln(\chi^2)$, for the cut $\chi^2_{i, max} = 6$, from Table 2 plotted against the cms energy, \sqrt{s} , in GeV. The data shown are the sieved data with $\sqrt{s} = 6$ GeV. The $\ln^2(\chi^2)$ tests with $\chi^2_{i, max} = 6$ corresponding to the solid curve for $p\bar{p}$ and the dash-dotted curve for $p\bar{p}$, are in excellent agreement with the cross section data. On the other hand, the $\ln(\chi^2)$ tests the long dashed curve for $p\bar{p}$ and the short dashed curve for $p\bar{p}$ although they fit in the low energy region almost identically to the $\ln^2(\chi^2)$ tests are very bad fits which clearly underestimate all of the high energy cross sections, leading to huge χ^2_{min} , and hence are ruled out.

Figure 3 shows the individual fitted χ^2 -values for $p\bar{p}$ and $p\bar{p}$ for $\ln^2(\chi^2)$ and $\ln(\chi^2)$, for the cut $\chi^2_{i, max} = 6$, from Table 2, vs. \sqrt{s} , the cms energy in GeV. The data shown are the sieved data with $\sqrt{s} = 6$ GeV. The $\ln^2(\chi^2)$ tests with $\chi^2_{i, max} = 6$, corresponding to the solid curve for $p\bar{p}$ and the dash-dotted curve for $p\bar{p}$, reproduce the data reasonably well. On the other hand, the $\ln(\chi^2)$ tests are rather poor.

Again the data offer firm support for the Froissart bounds, while ruling out $\ln(\sqrt{s})$ fits for the $p\bar{p}$ system.

Figure 4 shows an expanded scale of energies, in which all available $p\bar{p}$ cross sections are shown, from threshold to the highest available energies. The dashed curve is the even amplitude pion cross section $\frac{\sigma_{p\pi} + \sigma_{\pi p}}{2}$ computed from our $\sqrt{s}_{\text{max}} = 6$ cut, whereas the solid curve is the result of a similar analysis for the spin-averaged (even) cross section [6] for $p\bar{p}$ scattering, rescaled by multiplying it by 210, a familiar number from the vector dominance model. It is most striking that these two independent curves are virtually indistinguishable in the entire energy interval in which experimental data are available, i.e., $2 \leq \sqrt{s} \leq 300$ GeV — a result most strongly supporting the vector dominance model.

All known $p\bar{p}$ cross section data are plotted in Figure 5, which compares our analysis using the 4 constraint equations ($\sqrt{s}_{\text{max}} = 6$ from Table 2) with the analysis of Igi and Ishida [5] which used finite energy sum rules (FESR) for their low energy data. They only fitted the even cross section, so we have plotted in Fig. 5(a) the even portion of our $\ln^2(\sqrt{s})$ fit as the solid curve. It is seen to go smoothly through the average cross section, $\frac{\sigma_{p\pi} + \sigma_{\pi p}}{2}$, for pion-proton scattering. The dashed-dot curve, using the FESR, is from Igi and Ishida [5]. It does not go very smoothly through the average of the points, but rather goes much closer to $\sigma_{p\pi}$ in the energy region from 10 to 30 GeV. Perhaps this is the result of their trying to fit only the even cross section, whereas we separately fit $\sigma_{p\pi}$ and $\sigma_{\pi p}$. We have plotted in Fig. 5(b) the even portion of our $\ln(\sqrt{s})$ fit as the dashed curve, with the FESR result being the dashed-dot-dot curve. Clearly both curves rule out a $\ln(\sqrt{s})$ behavior. Both analyses strongly support a $\ln^2(\sqrt{s})$ behavior and thus a saturation of the Froissart bound for the $p\bar{p}$ system.

Figure 6 shows the individual fitted cross sections (in mb) for $p\bar{p}$ and $p\bar{p}$ for $\ln^2(\sqrt{s})$ and $\ln(\sqrt{s})$ for the cut $\sqrt{s}_{\text{max}} = 6$ in Table 3, plotted against the cms energy, \sqrt{s} , in GeV. The data shown are the sieved data with $\sqrt{s} \leq 6$ GeV. The $\ln^2(\sqrt{s})$ fits to the data sample with $\sqrt{s}_{\text{max}} = 6$, corresponding to the solid curve for $p\bar{p}$ and the dash-dotted curve for $p\bar{p}$, are excellent, yielding a total renormalized $\chi^2 = 201.5$, for 184 degrees of freedom, corresponding to a p -value probability of 0.2. On the other hand, the $\ln(\sqrt{s})$ fits to the same data sample — the long dashed curve for $p\bar{p}$ and the short dashed curve for $p\bar{p}$ — are very bad fits, yielding a total $\chi^2 = 2613.7$ for 185 degrees of freedom, corresponding to a p -value probability of $< 10^{-16}$. In essence, the $\ln(\sqrt{s})$ fit clearly undershoots all of the high energy cross sections. The ability of nucleon-nucleon scattering to distinguish cleanly between an energy dependence of $\ln^2(\sqrt{s})$ and an energy dependence of $\ln(\sqrt{s})$ is even more dramatic than the pion result.

Figure 7 shows the individual fitted χ^2 -values for $p\bar{p}$ and $p\bar{p}$ $\ln^2(\sqrt{s})$ and $\ln(\sqrt{s})$ from Table 3, using $\sqrt{s}_{\text{max}} = 6$ plotted against the cms energy, \sqrt{s} , in GeV. The data shown are the sieved data with $\sqrt{s} \leq 6$ GeV. The $\ln^2(\sqrt{s})$ fits, corresponding to the solid curve for $p\bar{p}$ and the dash-dotted curve for $p\bar{p}$, fit the data reasonably well. On the other hand, the $\ln(\sqrt{s})$ fits, the long dashed curve for $p\bar{p}$ and the short dashed curve for $p\bar{p}$, are very poor fits, missing completely the precise $p\bar{p}$ at 546 GeV, as well as $p\bar{p}$ at 1800 GeV. These results again strongly support the $\ln^2(\sqrt{s})$ fits that saturate the Froissart bound and once again rule out $\ln(\sqrt{s})$ fits for the $p\bar{p}$ and $p\bar{p}$ system.

A few remarks on our $\ln^2(\sqrt{s})$ asymptotic energy analysis for $p\bar{p}$ and $p\bar{p}$ are in order. It should be stressed that we used both the CDF and E710/E811 high energy experimental cross sections at $\sqrt{s} = 1800$ GeV in the $\ln^2(\sqrt{s})$ analysis, summarized in Table 3, $\sqrt{s}_{\text{max}} = 6$ and shown in Figures 6 and 7. Inspection of Fig. 6 shows that at $\sqrt{s} = 1800$ GeV, our fit effectively passes below the cross section point of 80 mb (CDF collaboration). In particular, to test the sensitivity of our fit to the differences between the highest energy accelerator $p\bar{p}$ cross sections from the Tevatron, we next omitted completely the CDF (80 mb) point and refitted the data without it. This fit, also using $\sqrt{s}_{\text{max}} = 6$, had a renormalized $\chi^2/\text{d.o.f.} = 1.055$, compared to 1.095 with the CDF point included. Since you only expect, on average, a χ^2 of 1 for the removal of one point, the removal of the CDF point slightly improved the goodness-of-fit. Moreover, the new parameters of the fit were only very minimally changed. As an example, the predicted value from the new fit for the cross section at $\sqrt{s} = 1800$ GeV — without the CDF point — was $\sigma_{p\bar{p}} = 75.1 \pm 0.6$ mb, where the error is the statistical error due to the errors in the fitted parameters. Conversely, the predicted value from Table 4 — which used both the CDF and the E710/E811 point — was $\sigma_{p\bar{p}} = 75.2 \pm 0.6$ mb, virtually identical. Further, at $\sqrt{s} = 14$ TeV (LHC energy), the fit without the CDF point had $\sigma_{p\bar{p}} = 107.2 \pm 1.2$, whereas including the CDF point (Table 4) gave $\sigma_{p\bar{p}} = 107.3 \pm 1.2$. Thus, within errors, there was practically no effect of either including or excluding the CDF point. The fit was determined almost exclusively by the

E710/E811 cross section | presumably because the asymptotic t was locked into the low energy transition energy s_0 , thus sampling the rich amount of lower energy data.

Our result concerning the (un)importance of the CDF point relative to E710/E811 result is to be contrasted with the statement from the COMPETE Collaboration[4] which emphasized that there is: "the systematic uncertainty coming from the discrepancy between different FNAL measurements of σ_{tot} ", which contribute large differences to their t predictions at high energy, depending on which data set they use. In marked contrast to our results, they conclude that their fitting techniques favor the CDF point. Our results indicate that both the cross section and ρ -value of the E710/E811 groups are slightly favored. More importantly, we find virtually no sensitivity to high energy predictions when we do not use the CDF point and only use the E710/E811 measurements. Our method of fitting the data | by anchoring the asymptotic t at the low transition energy s_0 | shows that our high energy predictions are quasi-independent of the FNAL "discrepancy", leading us to believe that our high energy cross section predictions at both the LHC and at cosmic ray energies are both robust and accurate. In Table 4, we give predictions | from our $\ln^2(\sqrt{s}/\sqrt{s_p})$ | for some values of σ_{pp} and ρ_{pp} at high energies. The errors quoted are due to the statistical errors of the fitted parameters c_1, c_2 and $f_+(0)$ given in the $\chi^2_{min} = 6, \ln^2(\sqrt{s}/\sqrt{s_p})$ of Table 3.

In Fig. 8, we show an extended energy scale, from threshold up to cosmic ray energies (1.876×10^5 GeV), plotting all available pp and pp cross sections, including cosmic ray pp cross sections inferred from cosmic ray p-air experiments by Block, Halzen and Stanov[11]. The solid curve is our result from Table 3 of the even cross section from $\ln^2(\sqrt{s}/\sqrt{s_p})$, $\chi^2_{min} = 6$. The dashed-dot-dot curve is from an independent QCD-inspired eikonal analysis[11] of the nucleon-nucleon system. The agreement is quite remarkable | the two independent curves are virtually indistinguishable over almost 5 decades of \sqrt{s} energy, from 3 GeV to 100 TeV. Figure 8 clearly indicates that the pp and pp cross section data greater than 3 GeV can be explained by a t of the form $\sigma = c_0 + c_1 \ln \frac{\sqrt{s}}{\sqrt{s_p}} + c_2 \ln^2 \frac{\sqrt{s}}{\sqrt{s_p}} + \rho \frac{\sqrt{s}}{\sqrt{s_p}} \frac{1}{\sqrt{s_p}}$ over an enormous energy range, i.e., by a $\ln^2 s$ saturation of the Froissart bound.

In Table 4, we make predictions of total cross sections and ρ -values for pp and pp scattering | in the low energy regions covered by RHIC, together with the energies of the Tevatron and LHC as well as the high energy regions appropriate to cosmic ray air shower experiments.

We give strong support to vector meson dominance by showing that the even cross section from our fits for π^+p and π^-p data agrees exceedingly well with a rescaled (multiplied by a factor of 210) ρ_p analysis done earlier by Block and Halzen [6], when both cross sections have a $\ln^2 s$ asymptotic behavior.

In conclusion, we have demonstrated that the duality requirement that high energy cross sections smoothly interpolate into the resonance region strongly favors a $\ln^2 s$ behavior of the asymptotic cross sections for both the πp and nucleon-nucleon systems, in agreement with our earlier result for πp scattering[6]. We conclude that the three hadronic systems, πp , π^-p and nucleon-nucleon, all have an asymptotic $\ln^2 s$ behavior, thus saturating the Froissart bound.

At 14 TeV, we predict $\sigma_{pp} = 107.3 \pm 1.1$ mb and $\rho_{pp} = 0.132 \pm 0.001$ for the Large Hadron Collider | robust predictions that rely critically on the saturation of the Froissart bound.

Acknowledgments

The work of FH is supported in part by the U.S. Department of Energy under Grant No. DE-FG02-95ER40896 and in part by the University of Wisconsin Research Committee with funds granted by the Wisconsin Alumni Research Foundation.

References

- [1] M .M .Block, physics/0506010 2005; submitted to Phys.Rev.D .
- [2] M .Froissart, Phys.Rev.123,1053 (1961).
- [3] M .M .Block, K .Kang and A .R .White, Int.J.Mod.Phys.A 7,4449 (1992).
- [4] J.R.Cuddelet al, Phys.Rev.D 65,074024 (2002);(COMPETE Collaboration) Phys.Rev.Letters,89,201801 (2002).
- [5] K .Igi and M .Ishida, Phys.Rev.D 66,034023 and references therein.
- [6] M .M .Block and F.Halzen, hep-ph0405174 (2004); Phys.Rev.D 70,091901 (2004).
- [7] M .M .Block and R.N.Cahn, Rev.Mod.Phys.57,563 (1985).
- [8] M .M .Block, Phys.Rev.D 65,116005 (2002).
- [9] For the reaction $\pi^+ p \rightarrow \pi^+ p$, it is fixed as the Thompson scattering limit $f_1(0) = \frac{1}{2}m_\pi^2 = 3.03 \text{ fb GeV}$; see M .Damashnek and F.J.Gilman, Phys.Rev.D 1,1319 (1970).
- [10] Particle Data Group, H .Hagiwara et al, Phys.Rev.D 66,010001 (2002).
- [11] M .M .Block, F.Halzen and T.Stanov, Phys.Rev.Lett.83,4926 (1999); Phys.Rev.D 62,077501 (2000).

Transition Energy Parameters	^+p and p Scattering	pp and pp Scattering
ϵ_0 , lab transition energy (GeV)	3.12	7.59
ϵ_0^+ , cms transition energy (GeV)	2.6	4
$\sigma^+(\epsilon_0)$ (mb)	28.91	40.18
$\sigma(\epsilon_0)$ (mb)	32.04	56.99
$\frac{d\sigma^+}{d(\epsilon - \epsilon_0)} = \sigma_0$ (mb)	-0.2305	-0.2262
$\frac{d\sigma}{d(\epsilon - \epsilon_0)} = \sigma_0$ (mb)	-1.446	-0.2740
Minimum fitting energy		
ϵ_{min} , lab minimum energy (GeV)	18.71	18.25
ϵ_{min}^+ , cms minimum energy (GeV)	6.0	6.0

m is the pion (proton) mass and ϵ is the laboratory pion (proton) energy

Table 1: The transition energy parameters used for fitting ^+p , p , pp and pp scattering.

Parameters	$\ln^2(\sqrt{s})$		$\ln(\sqrt{s})$
	χ^2_{max}		χ^2_{max}
	6	9	6
Even Amplitude			
c_0 (mb)	20.11	20.32	12.75
c_1 (mb)	0.921 0.110	0.981 0.100	1.286 0.0056
c_2 (mb)	0.1767 0.0085	0.1815 0.0077	
p^0 (mb)	54.40	54.10	64.87
	0.5	0.5	0.5
$f(0)$ (mb GeV)	2.33 0.36	2.31 0.35	0.34 0.36
Odd Amplitude			
(mb)	4.51	4.51	-4.51
	0.660	0.660	0.660
χ^2_{min}	148.1	204.4	941.8
$R \chi^2_{\text{min}}$	164.3	210.0	1044.9
(d.f.)	127	135	128
$R \chi^2_{\text{min}} =$	1.294	1.555	8.163

Table 2: The fitted results for a 3-parameter χ^2 fit with $\ln^2(\sqrt{s})$ and a 2-parameter fit with $\ln(\sqrt{s})$ to the total cross sections and ρ -values for ^+p and ^-p scattering. The renormalized χ^2_{min} , taking into account the effects of the χ^2_{max} cut, is given in the row labeled $R \chi^2_{\text{min}} =$. The errors in the fitted parameters have been multiplied by the appropriate r_2 . The pion mass is m_π and the laboratory pion energy is E_π .

Parameters	$\ln^2(\sqrt{s} m_p)$		$\ln(\sqrt{s} m_p)$
	$\sigma_{\text{in ax}}^2$		$\sigma_{\text{in ax}}^2$
	6	9	6
Even Amplitude			
c_0 (mb)	37.32	37.25	28.26
c_1 (mb)	1.440 0.070	1.416 0.066	2.651 0.0070
c_2 (mb)	0.2817 0.0064	0.2792 0.0059	
p^0 (mb)	37.10	37.17	47.98
	0.5	0.5	0.5
$f(0)$ (mb GeV)	0.075 0.59	0.069 0.57	4.28 0.59
Odd Amplitude			
(mb)	28.56	28.56	-28.56
	0.415	0.415	0.415
σ_{in}^2	181.6	216.6	2355.7
$R \sigma_{\text{in}}^2$	201.5	222.5	2613.7
(d.f.)	184	189	185
$R \sigma_{\text{in}}^2 =$	1.095	1.178	14.13

Table 3: The fitted results for a 3-parameter fit with $\ln^2(\sqrt{s} m_p)$ and a 2-parameter fit with $\ln(\sqrt{s} m_p)$ to the total cross sections and ρ -values for pp and pp scattering. The renormalized σ_{in}^2 , taking into account the effects of the $\sigma_{\text{in ax}}^2$ cut, is given in the row labeled $R \sigma_{\text{in}}^2$. The errors in the fitted parameters have been multiplied by the appropriate r_2 . The proton mass is m_p and the laboratory nucleon energy is \sqrt{s} .

\sqrt{s} , in GeV	pp, in mb	pp	pp, in mb	pp
6	48.97 0.01	0.087 0.008	38.91 0.01	0.307 0.001
60	43.86 0.04	0.089 0.001	43.20 0.04	0.079 0.001
100	46.59 0.08	0.108 0.001	46.23 0.08	0.103 0.001
300	55.03 0.21	0.131 0.001	54.93 0.21	0.130 0.002
400	57.76 0.25	0.134 0.002	57.68 0.25	0.133 0.002
540	60.81 0.29	0.137 0.002	60.76 0.29	0.136 0.002
1,800	75.19 0.55	0.139 0.001	75.18 0.55	0.139 0.001
14,000	107.3 1.2	0.132 0.001	107.3 1.2	0.132 0.001
16,000	109.8 1.3	0.131 0.001	109.8 1.3	0.131 0.001
50,000	132.1 1.7	0.124 0.001	132.1 1.7	0.124 0.001
100,000	147.1 2.0	0.120 0.001	147.1 2.0	0.120 0.001

Table 4: Predictions of high energy pp and pp total cross sections and ρ -values, from Table 3, $\ln^2(\sqrt{s} m_p)$, $\sigma_{\text{in ax}}^2 = 6$.

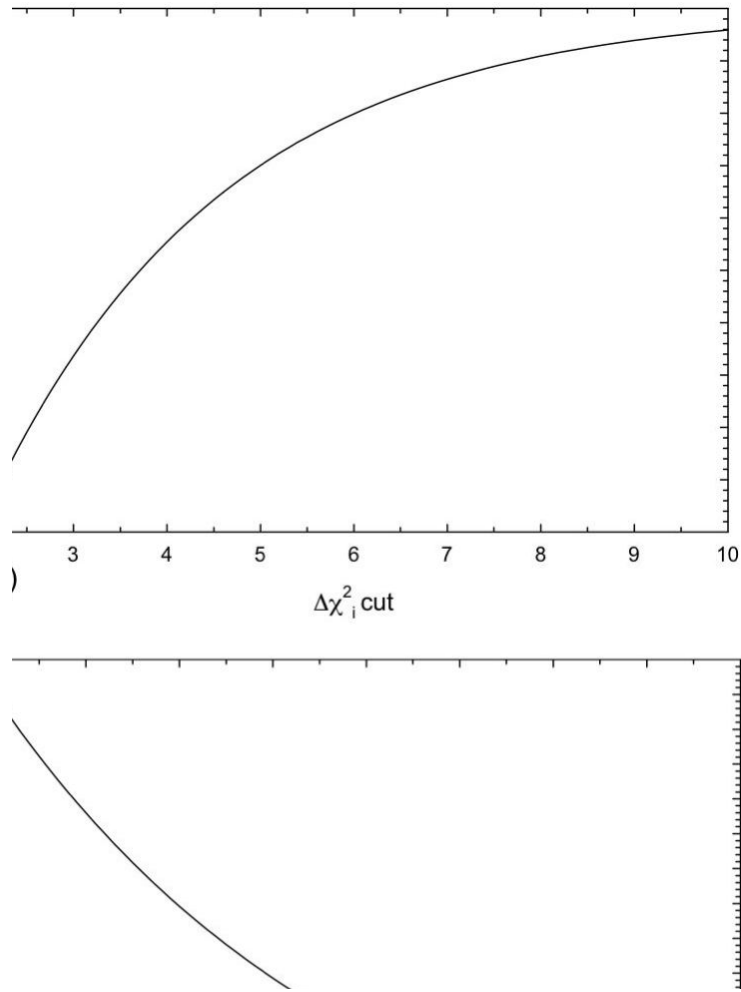


Figure 1: a) A plot of R^{-1} , the reciprocal of the factor that multiplies χ^2_{min} found in the χ^2 fit to the sifted data set vs. $\Delta\chi^2_i \text{ cut}$, i.e., χ^2_{imax} . b) A plot of r_2 , the factor whose square multiplies the covariant matrix found in the χ^2 fit to the sifted data set vs. $\Delta\chi^2_i \text{ cut}$, i.e., χ^2_{imax} . These figures are taken from ref. [1].

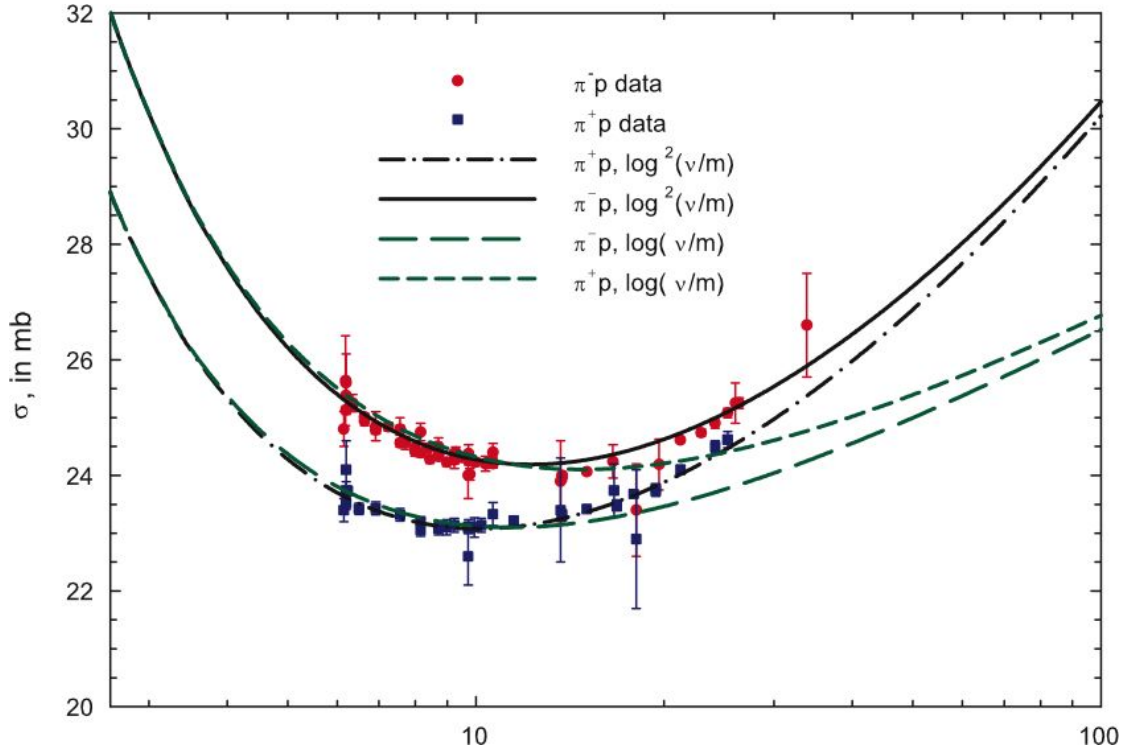


Figure 2: The fitted total cross sections σ_{π^+p} and σ_{π^-p} in mb, vs. \sqrt{s} , in GeV, using the 4 constraints of Equations (13), (14), (15) and (16). The circles are the sieved data for π^-p scattering and the squares are the sieved data for π^+p scattering for $\sqrt{s} \leq 6$ GeV. The dash-dotted curve (π^+p) and the solid curve (π^-p) are χ^2 fits (Table 2, $\chi^2_{\text{min}} = 6$) of the high energy data of the form: $\sigma_p = c_0 + c_1 \ln \frac{\sqrt{s}}{m} + c_2 \ln^2 \frac{\sqrt{s}}{m} + p_0 \frac{1}{m} \frac{1}{m}$. The upper sign is for π^+p and the lower sign is for π^-p scattering. The short dashed curve (π^+p) and the long dashed curve (π^-p) are χ^2 fits (Table 2, $\chi^2_{\text{min}} = 6$) of the high energy data of the form: $\sigma_p = c_0 + c_1 \ln \frac{\sqrt{s}}{m} + p_0 \frac{1}{m} \frac{1}{m}$. The upper sign is for π^+p and the lower sign is for π^-p scattering. The laboratory energy of the pion is \sqrt{s} and m is the pion mass.

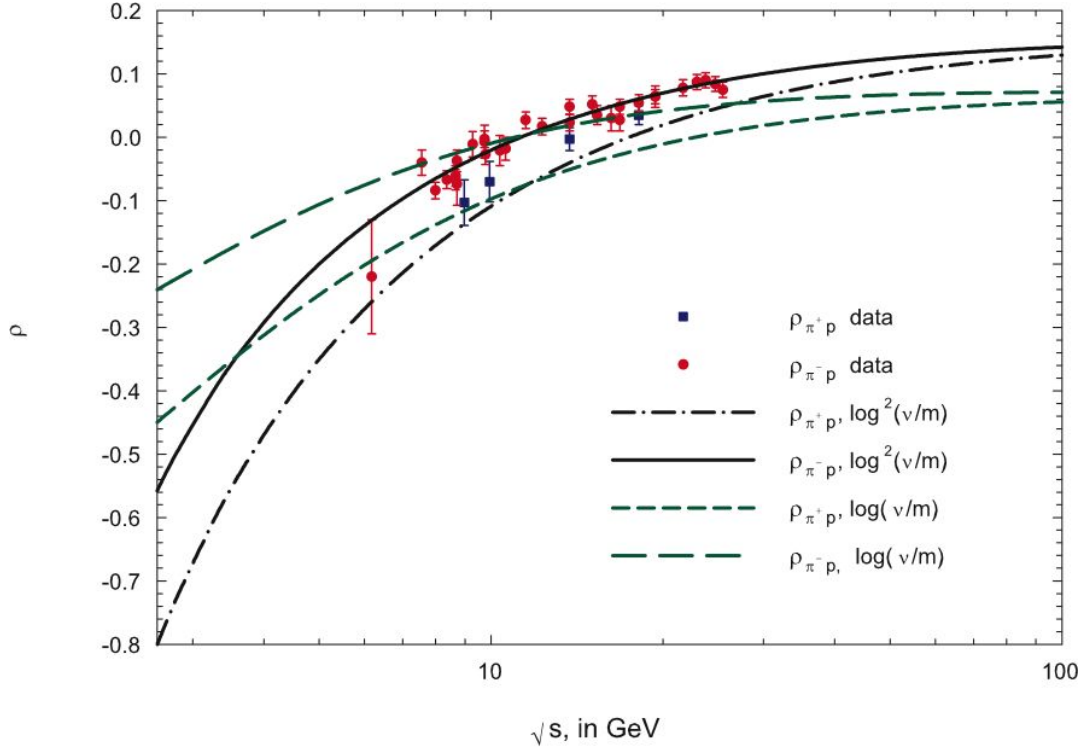


Figure 3: The fitted ρ -values, ρ_{π^+p} and ρ_{π^-p} , vs. \sqrt{s} , in GeV, using the 4 constraints of Equations (13), (14), (15) and (16). The circles are the sieved data for π^-p scattering and the squares are the sieved data for π^+p scattering for $\sqrt{s} \leq 6$ GeV. The dash-dotted curve (π^+p) and the solid curve (π^-p) are χ^2 fits (Table 2, $\chi^2_{\text{min}} = 6$) of the high energy data of the form : $\rho = \frac{1}{2}c_1 + c_2 \ln \frac{\sqrt{s}}{m} - \rho_0 \cot(\theta = 2) \frac{1}{m} + \frac{4}{m} f_+(0) \tan(\theta = 2) \frac{1}{m}$. The upper sign is for π^+p and the lower sign is for π^-p scattering. The short dashed curve (π^+p) and the long dashed curve (π^-p) are χ^2 fits (Table 2, $\chi^2_{\text{min}} = 6$) of the high energy data of the form : $\rho = \frac{1}{2}c_1 - \rho_0 \cot(\theta = 2) \frac{1}{m} + \frac{4}{m} f_+(0) \tan(\theta = 2) \frac{1}{m}$. The upper sign is for π^+p and the lower sign is for π^-p scattering. The laboratory energy of the pion is \sqrt{s} and m is the pion mass.

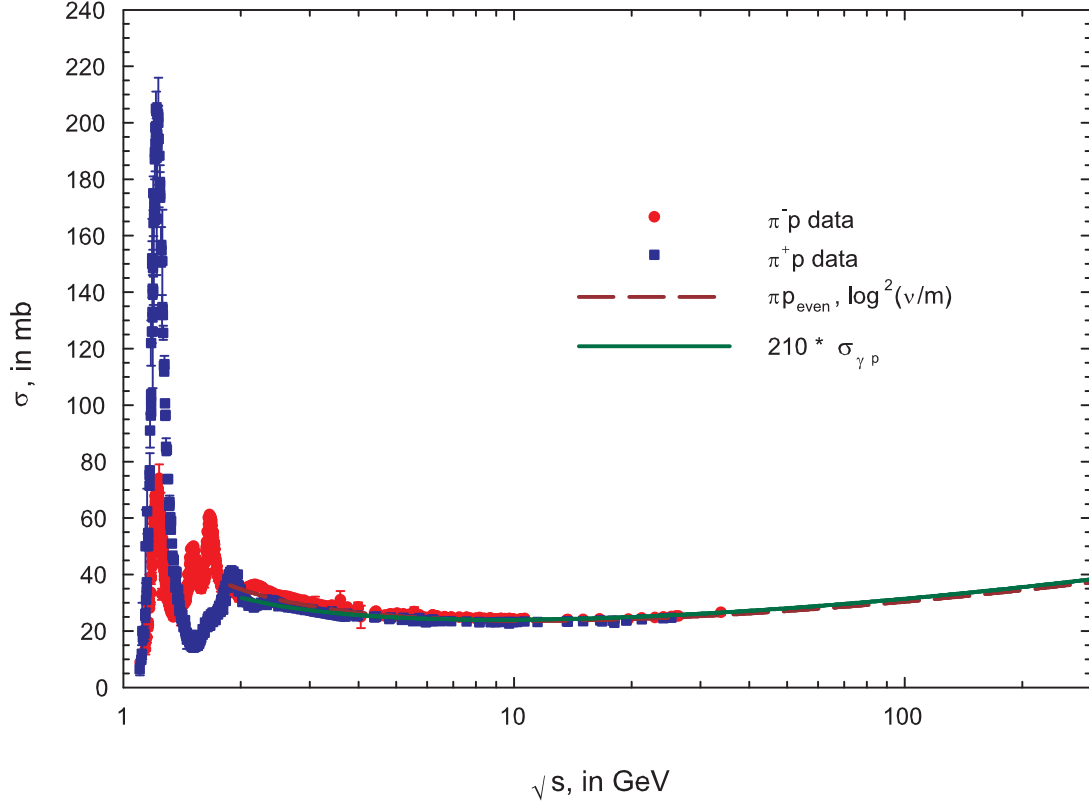


Figure 4: The circles are the cross section data for $\pi^- p$ scattering and the squares are the cross section data for $\pi^+ p$ scattering, in mb, vs. \sqrt{s} , in GeV, for all of the known data. The dashed curve is the π^2 fit (Table 2, $\ln^2(\sqrt{s}/m_\pi)$, $\ln^2_{\text{max}} = 6$) to the high energy cross section data of the even amplitude cross section, of the form : $\sigma_{\pi^{\pm} p \text{ even}} = c_0 + c_1 \ln \frac{\sqrt{s}}{m_\pi} + c_2 \ln^2 \frac{\sqrt{s}}{m_\pi} + \sigma_{\pi^0 p} \frac{m_p}{\sqrt{s}}$, with c_0 and $\sigma_{\pi^0 p}$ constrained by Eq.(13) and Eq.(14). The laboratory energy of the pion is E_{lab} and m_π is the pion mass. The dashed curve is $210 \sigma_{\gamma p}$, from a fit of γp cross sections by Block and Halzen [6] of the form : $\sigma_{\gamma p} = c_0 + c_1 \ln(\sqrt{s}/m_p) + c_2 \ln^2(\sqrt{s}/m_p) + \sigma_{\pi^0 p} \frac{m_p}{\sqrt{s}}$, where m_p is the proton mass. The γp cross sections were fit for cm s energies $\sqrt{s} = 2.01$ GeV, whereas the πp data (cross sections and χ^2 -values) were fit for cm s energies $\sqrt{s} = 6$ GeV. The two fitted curves are virtually indistinguishable in the energy region $2 < \sqrt{s} < 300$ GeV.

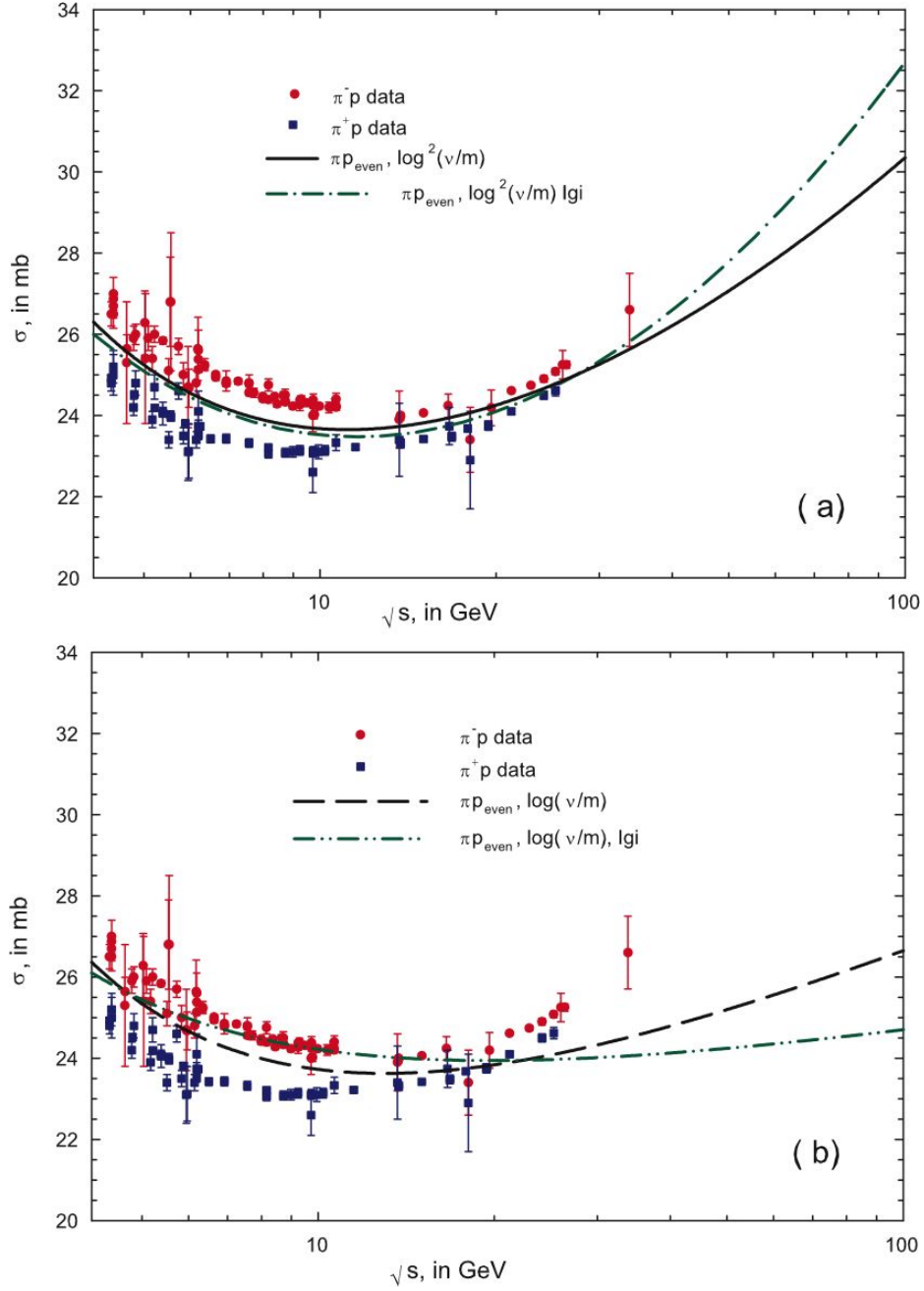


Figure 5: The circles are the cross section data for π^-p scattering and the squares are the cross section data for π^+p scattering for all known data, vs. \sqrt{s} , in GeV. The solid curve in Fig.(a) is the \log^2 fit (Table 2, $\ln^2(\sqrt{s}/m)$, $\ln^2_{\text{max}} = 6$) to the high energy cross section data of the even amplitude, of the form : $\sigma_{\text{even}} = c_0 + c_1 \ln \frac{\sqrt{s}}{m} + c_2 \ln^2 \frac{\sqrt{s}}{m} + \rho_0 \frac{1}{m}$, with c_0 and ρ_0 constrained by Eq. (13) and Eq. (14). The dash-dotted curve is an even amplitude $\ln^2(\sqrt{s}/m)$ fit made by Igi and Ishida[5], using finite energy sum rules (FESR). The dashed curve in Fig.(b) is the \log fit (Table 2, $\ln(\sqrt{s}/m)$, $\ln_{\text{max}} = 6$) to the high energy cross section data of the even amplitude, of the form : $\sigma_{\text{even}} = c_0 + c_1 \ln \frac{\sqrt{s}}{m} + \rho_0 \frac{1}{m}$, with c_0 and ρ_0 constrained by Eq. (13) and Eq. (14). The dot-dot-dashed curve is an even amplitude $\ln(\sqrt{s}/m)$ fit made by Igi and Ishida[5], using finite energy sum rules. The laboratory energy of the pion is \sqrt{s} and m is the pion mass.

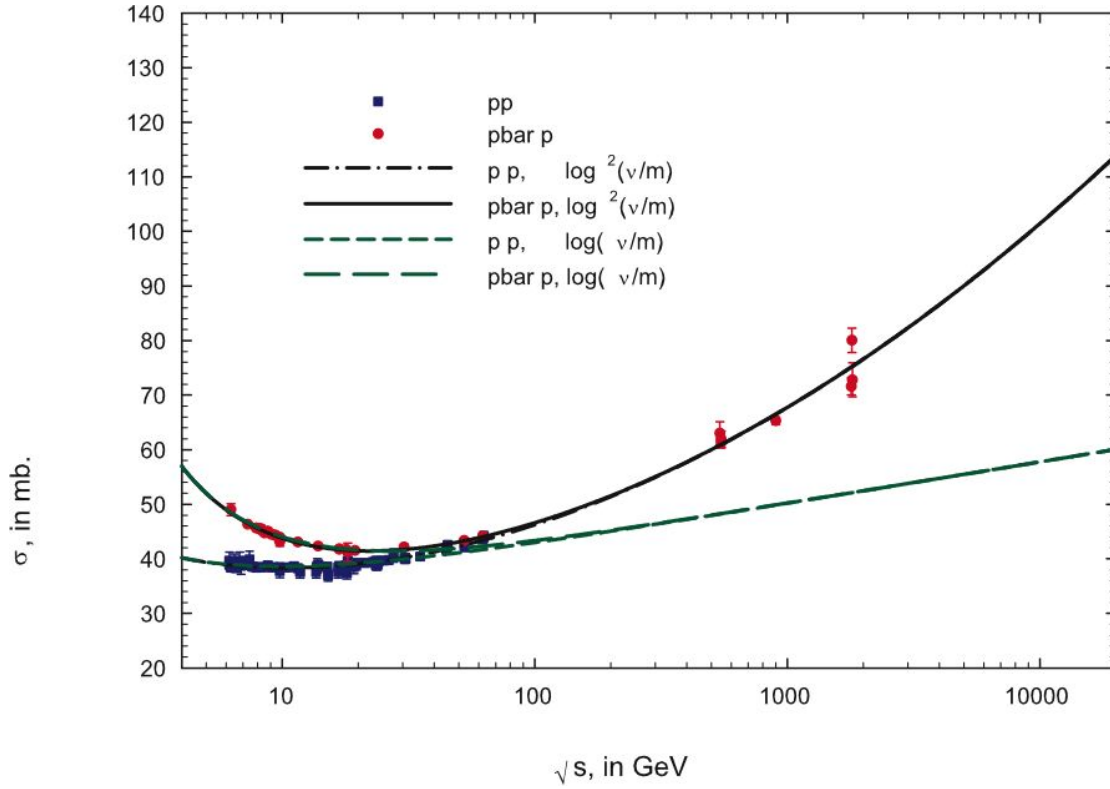


Figure 6: The fitted total cross sections σ_{pp} and $\sigma_{p\bar{p}}$ in mb, vs. \sqrt{s} , in GeV, using the 4 constraints of Equations (13), (14), (15) and (16). The circles are the sieved data for $p\bar{p}$ scattering and the squares are the sieved data for pp scattering for $\sqrt{s} \leq 6$ GeV. The dash-dotted curve ($p\bar{p}$) and the solid curve (pp) are \ln^2 fits (Table 3, $\chi^2_{\text{min}} = 6$) of the high energy data of the form : $\sigma = c_0 + c_1 \ln \frac{\sqrt{s}}{m} + c_2 \ln^2 \frac{\sqrt{s}}{m} + p_0 \frac{1}{m} \frac{1}{\sqrt{s}}$. The upper sign is for $p\bar{p}$ and the lower sign is for pp scattering. The short dashed curve ($p\bar{p}$) and the long dashed curve (pp) are \ln fits (Table 3, $\chi^2_{\text{min}} = 6$) of the high energy data of the form : $\sigma = c_0 + c_1 \ln \frac{\sqrt{s}}{m} + p_0 \frac{1}{m} \frac{1}{\sqrt{s}}$. The upper sign is for $p\bar{p}$ and the lower sign is for pp scattering. The laboratory energy of the nucleon is E_{lab} and m is the nucleon mass.

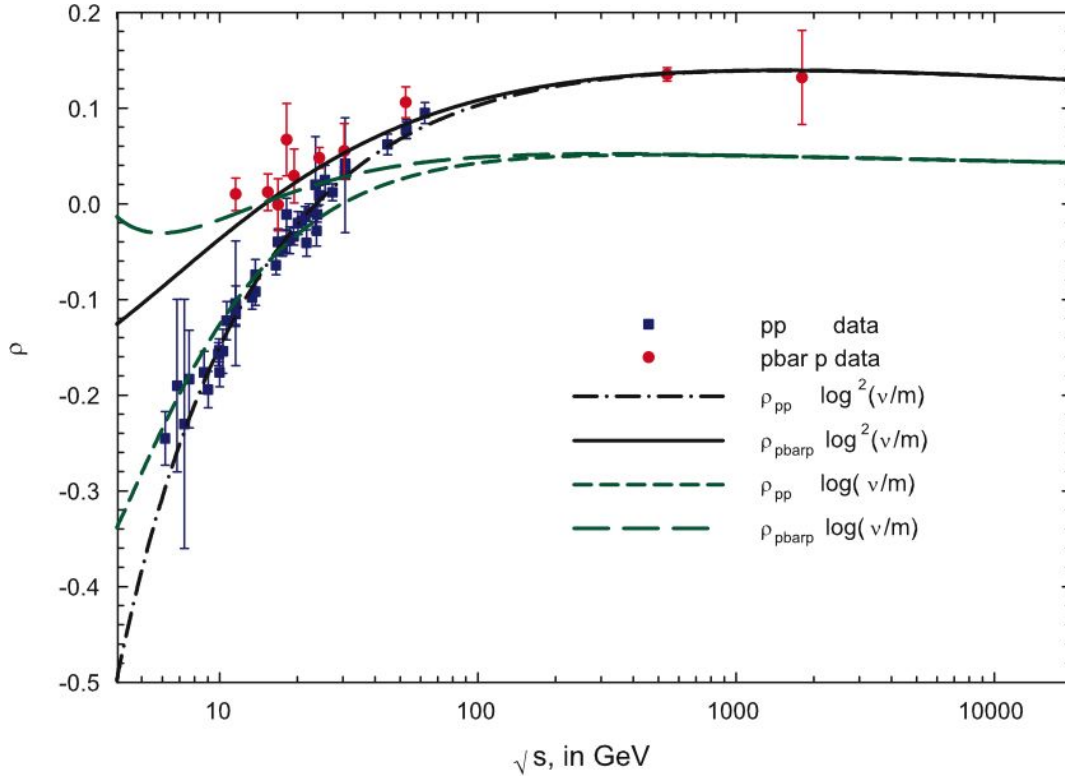


Figure 7: The fitted ρ -values, ρ_{pp} and $\rho_{p\bar{p}}$, vs. \sqrt{s} , in GeV, using the 4 constraints of Equations (13), (14), (15) and (16). The circles are the sieved data for $p\bar{p}$ scattering and the squares are the sieved data for pp scattering for $\sqrt{s} \geq 6$ GeV. The dash-dotted curve ($p\bar{p}$) and the solid curve (pp) are χ^2 fits (Table 3, $\chi^2_{\text{min}} = 6$) of the high energy data of the form : $\rho = \frac{1}{2}c_1 + c_2 \ln \frac{\sqrt{s}}{m} - \rho_0 \cot(\theta = 2) \frac{1}{m} + \frac{4}{m} f_+(0) \tan(\theta = 2) \frac{1}{m}$. The upper sign is for $p\bar{p}$ and the lower sign is for pp scattering. The short dashed curve ($p\bar{p}$) and the long dashed curve (pp) are χ^2 fits (Table 3, $\chi^2_{\text{min}} = 6$) of the high energy data of the form : $\rho = \frac{1}{2}c_1 - \rho_0 \cot(\theta = 2) \frac{1}{m} + \frac{4}{m} f_+(0) \tan(\theta = 2) \frac{1}{m}$. The upper sign is for $p\bar{p}$ and the lower sign is for pp scattering. The laboratory energy of the nucleon is E_{lab} and m is the nucleon mass.

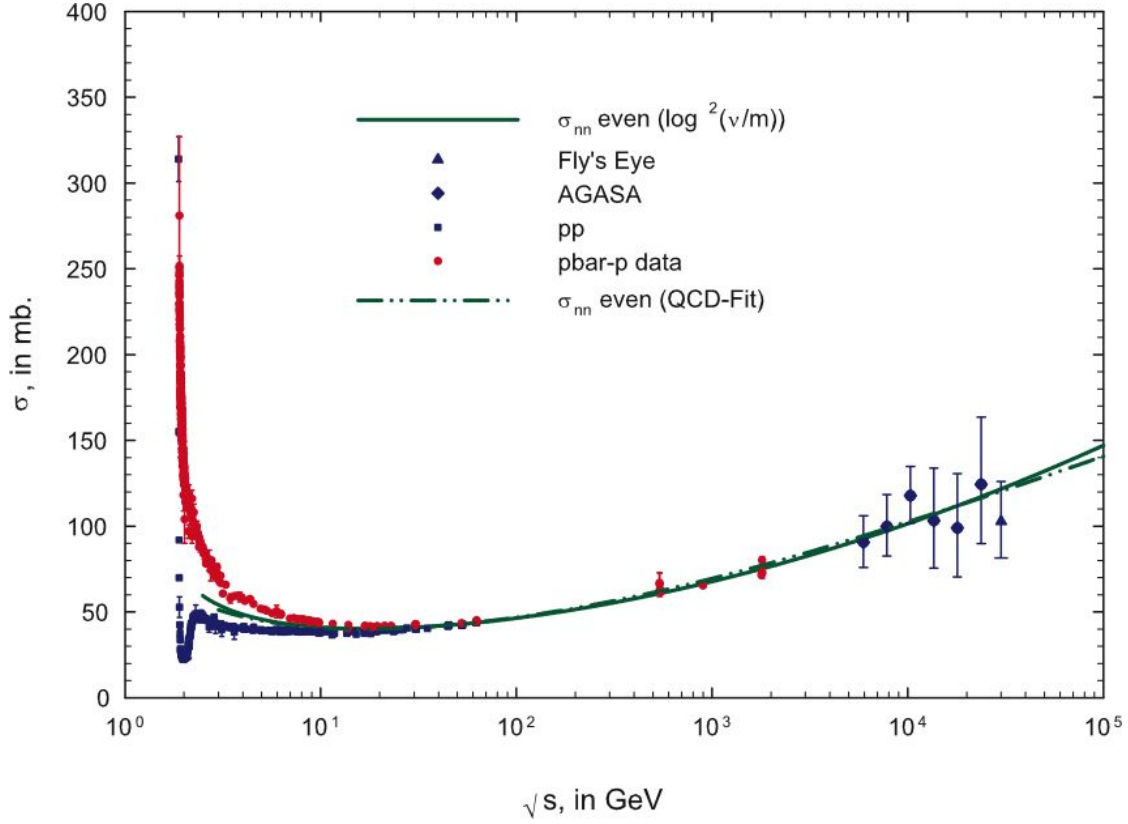


Figure 8: The circles are the cross section data for $p\bar{p}$ scattering and the squares are the cross section data for pp scattering, in mb, vs. \sqrt{s} , in GeV, for all of the known accelerator data. The solid curve is the \ln^2 fit (Table 3, $\ln^2(\sqrt{s}/m_p)$, $\ln^2_{\text{max}} = 6$) of the high energy data of the crossing-even amplitude, of the form: $\sigma_{nn\text{ even}} = c_0 + c_1 \ln \frac{\sqrt{s}}{m_p} + c_2 \ln^2 \frac{\sqrt{s}}{m_p} + p_0 \frac{1}{\sqrt{s}}$, with c_0 and p_0 constrained by Eq. (13) and Eq. (14). The dot-dot-dashed curve is the crossing-even amplitude cross section σ_{nn} , from a QCD-inspired fit that fits not only the accelerator pp and $p\bar{p}$ cross sections and α_s -values, but also fits the AGASA and Fly's Eye cosmic ray pp cross sections shown in the figure. Work done several years ago by the Block, Halzen and Stanov (BHS group) [11]. The laboratory energy of the proton is \sqrt{s} and m is the proton mass. It is most striking that the two fitted curves for $\sigma_{nn\text{ even}}$, using on the one hand, the $\ln^2(\sqrt{s}/m_p)$ model of this work and on the other hand, the QCD-inspired model of the BHS group [11], are virtually indistinguishable over 5 decades of cm s energy, i.e., in the energy region $3 \times 10^0 \leq \sqrt{s} \leq 10^5$ GeV.